iScience

CellPress
OPEN ACCESS

Article

First navigation with wireless muometric navigation system (MuWNS) in indoor and underground environments

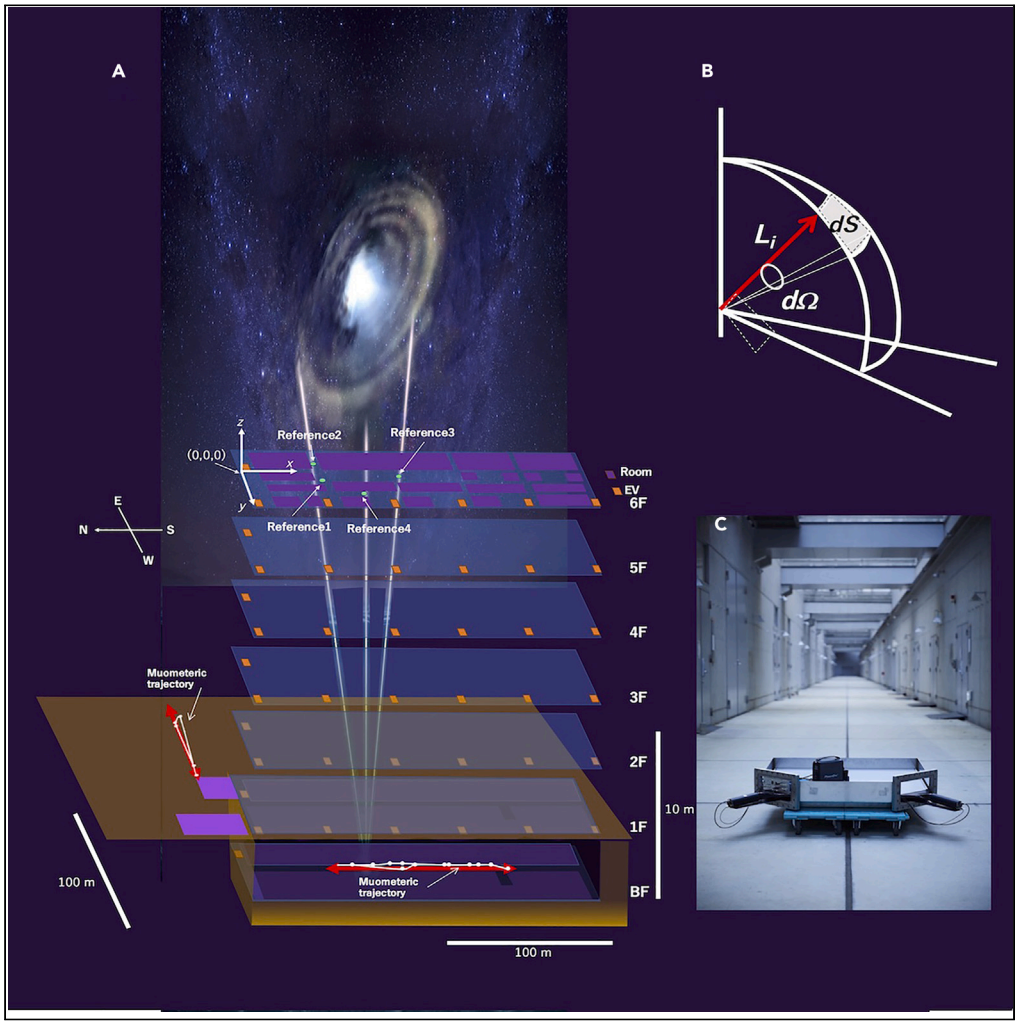

Hiroyuki K.M. Tanaka, Giuseppe Gallo, Jon Gluyas, ..., Yucheng Yang, Yusuke Yokota, muPS Collaboration

ht@eri.u-tokyo.ac.jp

Highlights

MuWNS enables indoor and underground navigation

MuWNS has been developed and demonstrated for the first time

Accuracy of the first prototype exceeded the GPS single-point positioning

Tanaka et al., iScience 26, 107000
July 21, 2023 © 2023
https://doi.org/10.1016/j.isci.2023.107000

iScience

CellPress
OPEN ACCESS

Article

First navigation with wireless muometric navigation system (MuWNS) in indoor and underground environments

Hiroyuki K.M. Tanaka,[1,2,8,*] Giuseppe Gallo,[2,3] Jon Gluyas,[2,4] Osamu Kamoshida,[2,5] Domenico Lo Presti,[2,3] Takashi Shimizu,[2,6] Sara Steigerwald,[2] Koji. Takano,[6] Yucheng Yang,[7] Yusuke Yokota,[1,2] and muPS Collaboration

SUMMARY

Navigation in indoor and underground environments has been extensively studied to realize automation of home, hospital, office, factory and mining services, and various techniques have been proposed for its implementation. By utilizing the relativistic and penetrative nature of cosmic-ray muons, a completely new wireless navigation technique called wireless muometric navigation system (MuWNS) was developed. This paper shows the results of the world's first physical demonstration of MuWNS used on the basement floor inside a building to navigate (a person) in an area where global navigation satellite system (GNSS)/global positioning system (GPS) signals cannot reach. The resultant navigation accuracy was comparable or better than the positioning accuracy attainable with single-point GNSS/GPS positioning in urban areas. With further improvements in stability of local clocks used for timing, it is anticipated that MuWNS can be adapted to improve autonomous mobile robot navigation and positioning as well as other underground and underwater practical applications.

INTRODUCTION

Autonomous mobile robots have been developed to efficiently undertake complex missions in indoor and underground environments. They have far-reaching application possibilities including automation of home, hospital, office, factory and mining (for example, emergency response, and security) services. However, determining a universal methodology for navigation and positioning is a major obstacle that must be overcome before practical implementations of autonomous mobile robots (or a myriad of other applications) can be realized. Thus far, many approaches have been tested such as cameras,[1–4] acoustic,[5] laser scanner,[6] dead reckoning (DR),[7,8] global navigation satellite system (GNSS)/global positioning system (GPS),[9] Wi-Fi,[10] Lidar,[11] etc. (usually in combination) to improve the positioning accuracy. Each technique has different pros and cons, and each technique performs best in a specific navigation environment. One of the most common techniques is to position the autonomous unit using cameras. Recent research has produced two fundamental camera-based techniques for indoor robot navigations: the grid-based (metric) method and the topological method. The grid-based framework (examples are FINALE[1] and Moravec[12]) requires a geometrical representation of space and relies on the camera image to pinpoint landmark features in the "vicinity" of the robot for determining its position. Another camera-based strategy is a navigation system, which uses a topological representation of space and an ensemble of neural networks to guide a robot through interior space (examples are NEURO-NAV[13,14] and FUZZY-NAV[15]). To give an example of the capabilities of these camera-based navigation techniques, FINALE can (equipped with a high-performance camera under optimal conditions) navigate a robot in motion at an average speed of 17 m/min using an ordinary Personal-computer-(PC)-based self-positioning algorithm that processes images based on camera data. However, errors accumulate as the time span of the robot navigation session lengthens, and repeated corrections with an external device are necessary for satisfactory performance.[4,16,17] Moreover, since these methods estimate the location of the robot based on the observation of landmarks established in the environment,[4,17] these techniques cannot be used when the landmarks are not observable, for example, in low-lighting conditions or in an environment where ambient light and shielding obstacles would compromise the ability of cameras to accurately render landmarks. The satellite-based navigation system known as GNSS or GPS is widely used to navigate moving objects located outdoors. However, GPS/GNSS receivers cannot be used in the indoor or underground environments. Radio frequency

[1]The University of Tokyo, Tokyo, Japan

[2]International Virtual Muography Institute (VMI), Global, Tokyo, Japan

[3]University of Catania, Catania, Italy

[4]Durham University, Durham, UK

[5]NEC Corporation, Tokyo, Japan

[6]Technoland Corporation, Tokyo, Japan

[7]Peking University, Beijing, China

[8]Lead contact

*Correspondence: ht@eri.u-tokyo.ac.jp

https://doi.org/10.1016/j.isci.2023.107000

identification (RFID) and ZigBee technologies can respectively achieve positioning accuracies of 10–30 m and 10–200 m[10] with a small battery consumption. However, RFID requires the establishment of a control center that contains servers, printers, monitors, and other components, and ZigBee requires a large-scale Wi-Fi network with a number of nodes. Dead reckoning (DR)[7,8] is often utilized as an indoor positioning algorithm, which allows users to estimate the total distance traveled from a starting point. Its drawback is that DR estimation errors also accumulate over time if no external reference signals are employed for correction. In order to transcend some of these limitations and based on calculations, Tanaka[18] proposed a completely new cosmic-ray muon probe-enabled indoor and underground navigation system. The original wired system is called the muometric positioning system (muPS), and there is also a recently proposed wireless-type muPS called wireless muometric navigation system (MuWNS).[19] The purpose of this paper is to report the results of the world's first physical indoor and underground navigation experiment with MuWNS. The current work focuses on about meter-sized objects navigating under several water-equivalent-meters of material, in a situation where one can install a reference detector at the surface. Although the method we discuss in this work might be generalizable, this spatial scale is the focus of our navigation in this work.

Traveling into and beyond the surface of every part of the Earth, the cosmic-ray muon is an abundant natural resource, which is utilized by muPS and MuWNS. These particles are produced in the Earth's atmosphere from galactic cosmic rays (GCRs). Generated from highly energetic events such as supernovae, GCRs will typically travel vast distances in outer space as they are deflected by local magnetic fields before colliding with matter; if they collide with nuclei in the Earth's atmosphere, mesons are generated. They eventually decay into muons. As the arrival angle of the GCR will determine the volume of matter in the atmosphere that the secondary particles (including muons) will encounter, the secondary particle's flux and average energy depend on their arriving angles; mesons (as secondary particles of GCRs) traveling through lower-density atmosphere tend to decay more prior to further interactions with atmospheric nuclei, and traversing through more matter increases the possibility of energy loss and vice versa. As a result, the vertical muon flux (the number of muons that are detected) tends to be higher than the horizontal muon flux. However, since lower-energy muons in the horizontal flux are more likely to decay, there tends to be a higher proportion of high-energy muons at horizontal angles. High-energy muons can reach speeds near the speed of light and adopt relativistic qualities. This lengthens their lifespan and makes it possible for these muons to survive long enough to penetrate into the surface of the Earth, underneath the Earth, and also underwater. Additionally, the muon is subjected to less radiative energy loss processes (Bremsstrahlung, direct pair production, and photonuclear interaction) than electrons; these factors further contribute to its penetrative nature. These unique qualities of muons have been utilized by muography, a technique which uses the muon as a probe to image the internal structure of geological objects and has been applied to various volcanoes including Asama volcano,[20] Usu volcano,[21] Sakurajima volcano,[22–24] Vesuvio volcano,[25] Stromboli volcano,[26] Etna volcano,[27] Satsuma-Iwojima volcano,[28] La Soufriere volcano,[29] and Puy de Dome volcano,[30] cultural heritage targets including a pyramid,[31,32] an underground ruin,[33–35] and time synchronization.[36] MuWNS and muPS are more recent new techniques which also utilize the muon probe.

The muometric positioning system (muPS) was invented as an underground and underwater positioning system, originally envisioned as a system ideally suited to detect seafloor deformation caused by submarine volcanism or plate tectonics.[18] The principle of the muPS technique is similar to the GNSS/GPS-based technique, which derives the receiver's position within the reference coordinates defined by multiple reference detectors instead of satellites by solving the following 4-fold equation:

$$L^2{}_i=(x_i-x_p)^2+(y_i-y_p)^2+(z_i-z_p)^2+s^2 \qquad \text{(Equation 1)}$$

where x_i, y_i, and z_i are the positions of the reference detectors, x_p, y_p, and z_p are the position of the receiver detector, and s (= $c\Delta t$) is the pseudo-length that comes from the time offset at the receiver detector. In the original muPS system, the reference detectors and the receiver detector are connected with wires to attain positioning accuracy at the centimeter scale. However, due to cable strain and entanglement risks, the cable inherently limits the mobility of the receiver detectors; therefore, this technique is more applicable to accurate monitoring of slow-moving objects such as seafloor deformation. Wireless MuWNS was designed to overcome the risks and limitations of the wired system to make muPS more flexible and adaptable to a wider-range of applications.[19] Cables connecting reference detectors with the receiver detector are not

used in the MuWNS system. This new capability would be useful in several cases. For example, as mentioned previously, this system adapts well as a solution for better navigation of remote-controlled robots. With muometric navigation (either wired or wireless), the time resolution of navigation is limited to the muon rate. Moreover, with MuWNS, since local clocks (instead of wires) are used for synchronization of the reference detectors and the receiver detector, the local clock's intrinsic jitter and drift are added as a degradation factor affecting the positioning accuracy. We can assume that the signal arrives to the receiver from multiple satellites at the same time when using GNSS/GPS-based positioning so that the 4-fold equations in Equation 1 can be solved to derive their four parameters (x, y, z, and Δt). On the other hand, since the open-sky muon flux is limited to $\sim 10^2$ muons $m^{-2}s^{-1}sr^{-1}$ for MuWNS experiments, any strong drift level associated with local clocks, (namely, when Δt varies with time) would make the 4-fold equation in Equation 1 no longer applicable. Tanaka[19] numerically modeled the oven-controlled-crystal-oscillator-based (OCXO-based) MuWNS and found that the positioning accuracy tends to fluctuate between 1 and 10 m, depending on the distance between the reference detectors and the receiver detector, detector size, and surrounding material density. In shallow underground environments, since the solid angles (Ω in Equation 2) formed between the reference detectors and receiver detector tend to be large, high-frequency muons could be used for navigation with a given-sized detector; hence frequent clock calibration is possible by frequently solving Equation 1. As a result, the drift effect associated with the receiver detector is continuously corrected; hence higher navigation accuracy is attainable. On the other hand, in deeper underground environments, in addition to the effect from smaller solid angles, muon flux at the receiver is further reduced. As a result, the muon tracking frequency is significantly reduced; hence the clock is less frequently calibrated, leading to lower navigation accuracy. The navigation accuracy is determined by the distance between the reference detector and the receiver detector and the amount of material existing between the reference detector and the receiver detector. Assuming the space between the reference detectors and the receiver detectors is fully packed with solid rock, in order to attain positioning accuracies of $\sim$1 m and $\sim$10 m, the soil thickness must be thinner than 15 m and 100 m, respectively.[19]

Most cosmic-ray muons travel faster than light in water. 90% of the open-sky muons which reach sea level have energies above 700 MeV. They travel faster than 0.99c through any kind of media as long as their energies are above 700 MeV. The accuracy of muometric positioning is in principle (disregarding issues of jitter associated with detectors, electronics, and local clocks) better than that of other underground/underwater positioning techniques. In this work, the goal was to design a real-life experiment to attain a targeted positioning accuracy comparable with the accuracy attainable with single-point GPS/GNSS positioning with MuWNS. Although the expected horizontal positioning accuracy of single-point GNSS positioning is 10–200 m with a dual frequency receiver,[37] compared to relative GNSS positioning, single-point positioning is efficient, fast (an attainable sampling rate of 1 Hz) and low cost (<1,000 US dollars), and widely used for urban navigation. In the current work, as the first step for a physical demonstration of MuWNS and bearing in mind the performance of GNSS/GPS, we aimed at a positioning accuracy of $\sim$10 m. This paper reports the first results of a real-world underground navigation experiment with MuWNS.

RESULTS

Principle

The principle of muPS is simple. The three-dimensional position of the receiver detector can be derived by solving Equation 1 which is also used for GPS (Figure 1A). The condition for solving Equation 1 requires an assumption that the expected values in all of the four parameters (x, y, z, and t) must be the same among these four equations; otherwise the four-fold equations in Equation 1 do not hold. This assumption is reasonable only when x, y, z, and t do not change significantly within the time required for collecting four muon tracks. However, unlike GPS signals, since cosmic-ray muons are spatiotemporally dispersed, these muons arrive at the reference detectors and the receiver detector sporadically, namely, they do not arrive at all the reference detectors and the receiver detector at the same time.

The number of muons (N) that are detected both with the reference detector and the receiver detector is a function of the solid angle (Ω) formed by the reference and receiver detectors. If the area of the small detectors (dS) and the distance (L_i) between the reference and the receiver detectors are given, the small solid angle ($d\Omega$) (Figure 1B) is approximated as:

$$d\Omega \sim dS L_i L_i^{-2} \text{ for } dS \ll L_i L_i^2 \qquad \text{(Equation 2)}$$

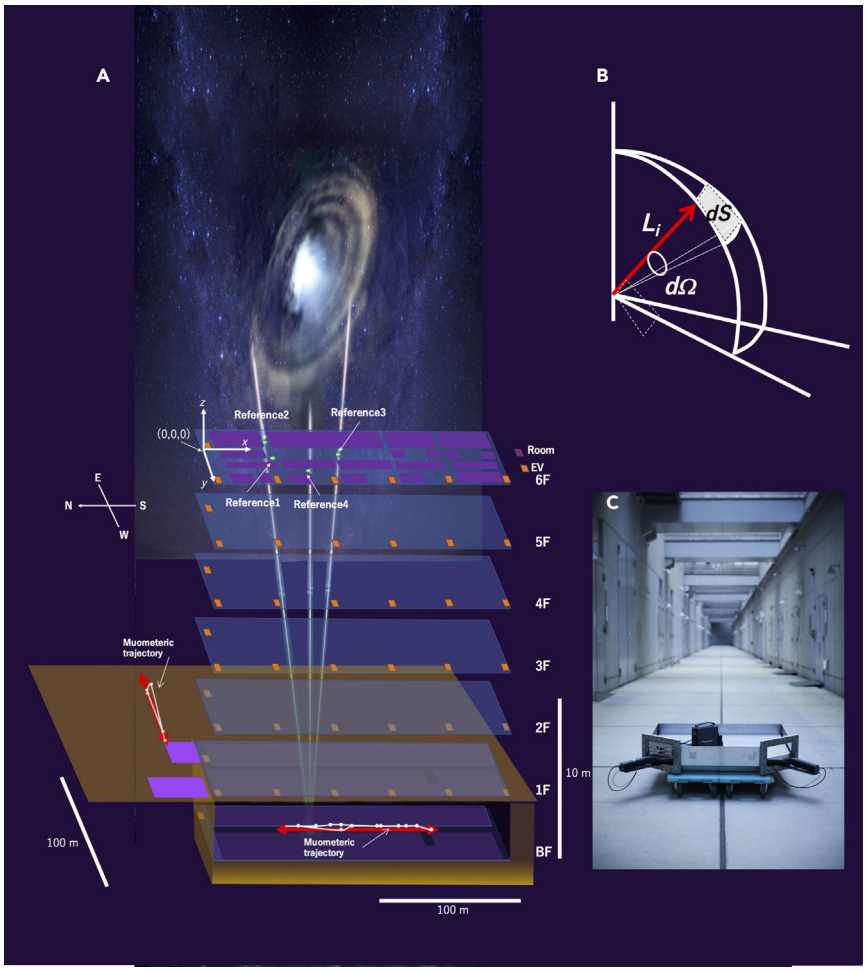

Figure 1. Conceptual view of the current muometric navigation in underground/indoor envirionments

(A–C) Structure of the building (Institute of Industrial Science, University of Tokyo) used for the current work is shown (A). Labels Reference 1 – Reference 4, EV, and muometric trajectory respectively indicate the first to fourth reference detectors, an elevator, and the muometrically determined path in the current work. The origin of coordinates (0, 0, 0) is also shown. Lines arriving from the galaxy indicate the muon trajectories. These lines are not representing particles directly arriving from the galaxy but representing that the muons used in this work are originated in galactic cosmic rays. The small solid angle formed by the reference detector and the receiver detector is shown (B). The notations are given in the main text. A photograph shows the receiver detector located in the corridor on the basement floor (C).

Therefore, the time (t_{min}) required for collecting the minimum number of muon tracks (four muon tracks) required for muPS will be:

$$t_{min}^{-1} = k I_{\mu} L_i^3 D^{-2} \quad \text{(Equation 3)}$$

where I_{μ} is the open-sky muon flux, and k is the reduction factor due to the muon's transmission through matter before arriving at the receiver detector, which is given by:

$$k = \left[\int_{Ec}^{\infty} I(E,\theta)dE\right]\left[\int_{0}^{\infty} I(E,\theta)dE\right]^{-1} \quad \text{(Equation 4)}$$

For example, if the sizes of the reference detectors and receiver detector are all 1 m^2, and if the distance between these detectors is 30 m, then t_{min} would be 10 s. If the navigatee travels at a walking speed (1 ms^{-1}), this time resolution (10 s) generates a positioning accuracy of 10 m; conversely, if the local clock fluctuates by 100 ns within 10 s, this jitter generates a positioning uncertainty of 30 m. In order to suppress this error associated with the muon arrival frequency, the speed of the navigatee was set to be a half of a

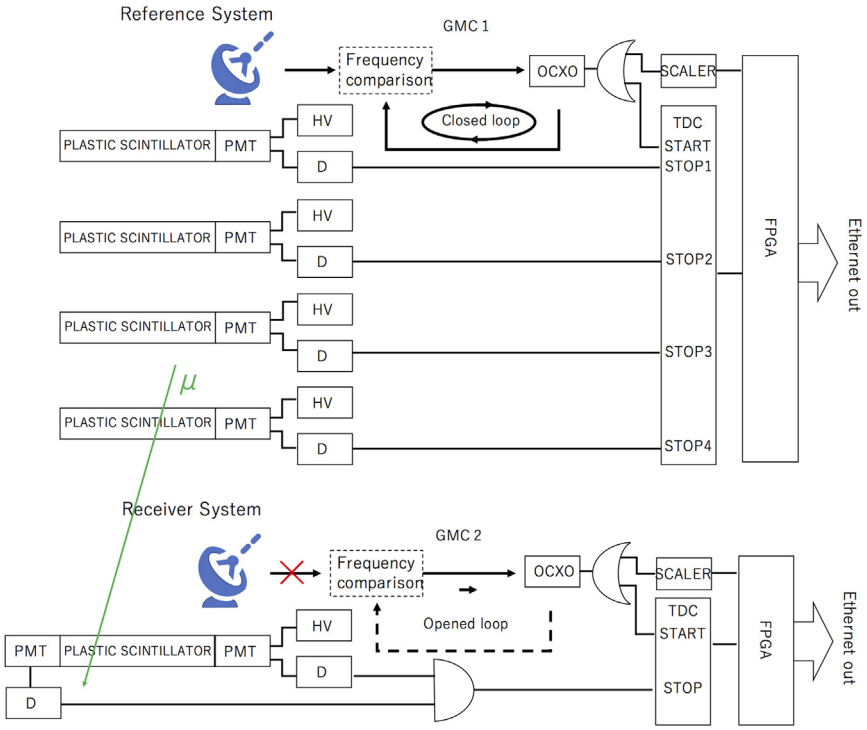

Figure 2. Block diagrams of the current wireless muometric navigation system

The diagrams are shown for the reference system (top panel) and the receiver system (bottom panel). Labels PMT, HV, D, OCXO, GMC, TDC, and FPGA respectively indicate a photomultiplier tube, a high voltage power supply, a discriminator, an oven-controlled crystal oscillator, a grandmaster clock, and a field programmable gate array. A red cross mark indicates disconnecting the system from the GPS antenna. A symbol μ indicates a muon.

regular walking speed (0.5 ms^{-1}), and the sixth floor was chosen for the locations of the reference detectors. Four reference detectors were placed on the sixth floor (green filled circles in Figure 1A), and each was labeled as the first, second, third, and fourth reference detectors respectively (see the configuration of reference 1-4 in Figure 1A). The vertical displacement between the basement and the receiver detector was 24 m, and the vertical displacement between ground level and the receiver detector was 20 m.

MuWNS

The current MuWNS consists of the following components: the detector, the grandmaster clock (GMC) (Trimble Thunderbolt PTP GM200),[38] and the associated electronics. A block diagram of the current navigation system is shown in Figure 2. Four reference detectors and one receiver detector comprise the detector system and included in each of the detectors are 1 × $1m^2$ square-shaped plastic scintillators with a thickness of 2 cm and photomultiplier tubes (PMTs) (Hamamatsu R7724) that are connected to each corner of each detector via an acrylic light guide unit. A redundant PMT is attached to the receiver detector to reduce the accidental coincidence rate, which originates from the PMT's dark current. The GMC component consists of two GMCs (GMC1 and GMC2) that are used for the measurements of the muon's time of flight (TOF) between the reference detectors and the receiver detector. GMC1 is associated with the reference detectors, and GMC2 is associated with the receiver detector. Each GMC consists of a GPS/GNSS receiver (multi-constellation GPS/GLONASS/Beidou/Galileo/QZSS) and an OCXO (Trimble OCXO) with a drift adjustment function and holdover function. The drift adjustment function corrects the OCXO's frequency drift in real time by frequency synchronization with GPS signals (See Figure 2A). These data can be used for "holding-over" its timing accuracy when the GMC is cut off from the GPS antenna. Therefore, the longer the GMC can operate in the GPS antenna mode, the better its time accuracy when no longer connected. Figure 3 shows the time-dependent GMC's drift level as a function of time after its cutoff phase from the GPS antenna in the holdover mode (see the Method section for the experimental setup which was used to collect these data). The associated electronics consist of high-voltage (HV) supplies, discriminators, the scaler electronics, and the time to digital converter (TDC). The current TDC time resolution is 27 ps.[18] Single count rates

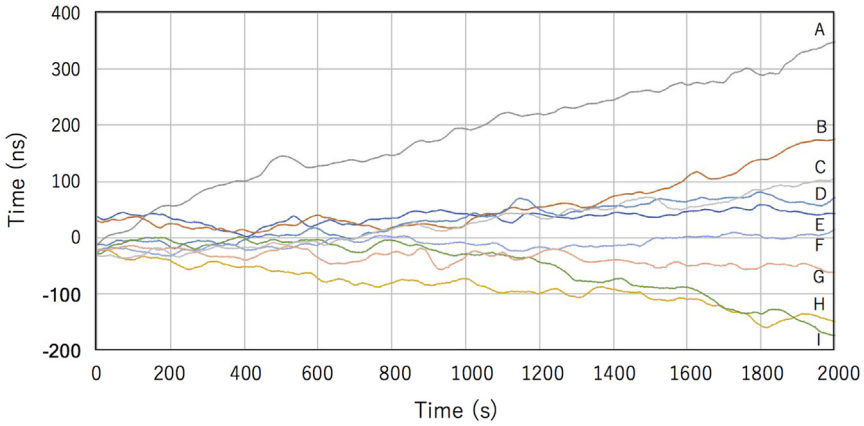

Figure 3. Time-dependent OCXO's drift level for different connection times before disconnection from the GPS antenna: A, 48 h, B, 72 h, C, 10 min, D, 0.5 h, E, 0 h (no antenna connections), F, 16 h, G, 8.5 h, H, 16 h, and I, 1 h

of the reference detectors and the receiver detector were all $\sim 10^2$ Hz. HV is applied to PMTs, and discriminators are used for binarizing PMT outputs. The purpose of the scaler electronics is to count the number of pulses outputted from the GMC, and the TDC measures the time difference between the muon arrival time and the timing of the GMC pulse outputs. More specifically, the GMC pulses are fed into the scaler electronics to measure and output the value of nT, where n is the number of the GMC pulses counted after the start of the measurement, and T is the period of the GMC pulses. The GMC pulses are also divided by a fan-out circuit to the TDC as the start signal. The discriminated PMT signals are fed into the TDC as the stop signal to output Δt, where Δt is the time displacement between the start and stop signals fed to the TDC. The scaler data and the TDC data are transferred to a field programmable gate array (FPGA) to merge these data. As a consequence, the resultant $nT + \Delta t$ indicates the time when the muon arrives at the detectors, where zero (as a unit of time) is defined by the resetting time of the TDC. The necessity of resetting the TDC is explained as follows. Even though the GMCs are connected to GPS antennas, two independent GMCs do not output identical times (see variations in the timing by the GMC clocks at time zero in Figure 3). Therefore, it is necessary to label the GMC pulse outputs as "time zero" to synchronize GMC1 and GMC2 on the timeline so that the same time is shared with these two GMCs. In order to do this, a reset signal is sent to two sets of scaler electronics at the same time to clear out the data accumulated in the GMC-TDC so that they can initiate counting the number of GMC pulses at the same time. The FPGA output data are transferred to the local PCs attached to the reference detectors and receiver detector so that $(nT + \Delta t)_{REFERENCE}$ and $(nT + \Delta t)_{RECEIVER}$ can be compared. In the reference manual of Trimble Thunderbolt PTP GM200, it was suggested to connect the clock with the GPS antenna for more than a few hours. However, as shown in Figure 3, the measurement result indicated that there is no correlation between the connection time and the drift level within the timescale we are discussing here (2,000 s). The measurements of this time-dependent OCXO's drift level were conducted in the following way. The PPS signals from the OCXO connected to a GPS antenna (OCXO1) and the OCXO disconnected from a GPS antenna (OCXO2) were both converted to the NIM level to be transferred to the TDC (Sciosence TDC-GPX) as a start and stop signals, respectively. Since both positive and negative drifts were expected, a delay circuit was inserted between OCXO2 and the TDC. The signals from the TDC were transferred to a CPLD and subsequently transferred to Raspberry Pi for communication to the local PC via Ethernet. The measurable time range of the TDC was 10 us with a resolution of 27 ps, and the minimum receivable pulse width was 10 ns.

In the current measurements, GMC1 is continuously connected with the GPS antenna and GMC2 is connected with the GPS antennas for more than 1 h prior to the muometric measurement to suppress the drift level as much as possible. The procedure of the current muometric measurement can be summarized as follows: (1) GMC1 and GMC2 are connected with the GPS antennas. (2) Right before navigation, GMC2 is disconnected from the GPS antennas. (3) After muometric measurements are completed, GMC2 is connected again to the GNSS antennas. The (2)-(3) processes were repeated in this work. The time required for the (2)-(3) processes was 30 min, and the current MuWNS was operated with 12-V batteries used for powering a laptop computer.

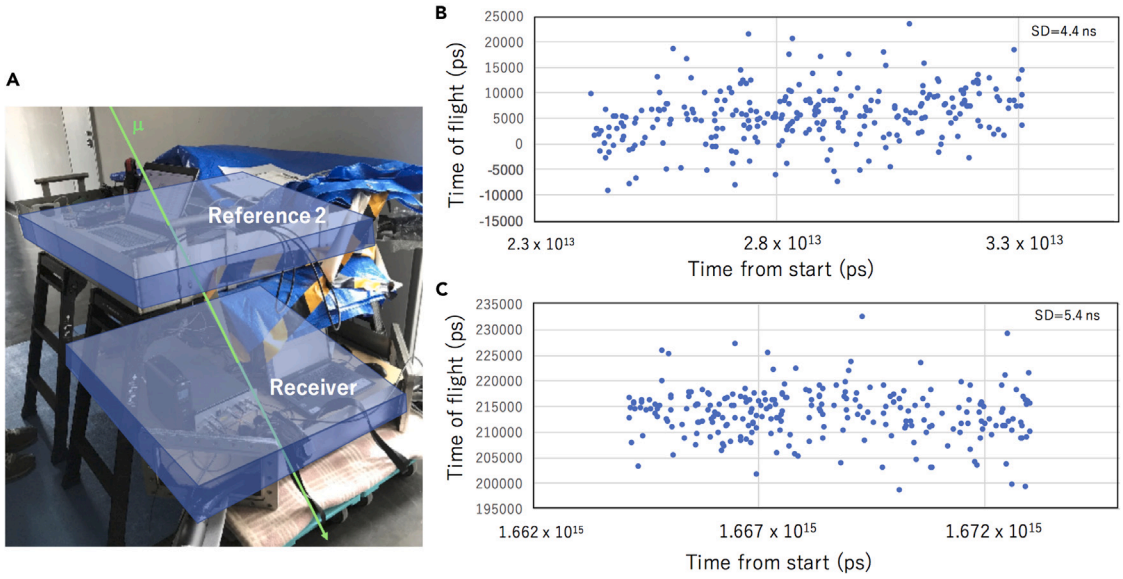

Figure 4. Time of flight (TOF) of muons at the initial position

(A–C) A photograph of the initial position of the receiver detector is shown (A). The labels "Reference 2" and "Receiver" respectively indicate the second reference detector and the receiver detector. The time sequential plots of the muon's TOF between reference 2 and receiver are shown for different periods of time: 23–33 s after starting the measurements (B) and 1,662-1,672 s after starting the measurements (C). The apparent difference in TOF between (B) and (C) comes from the OCXO's frequency drift and was used as the calibration data.

Experimental configuration

The subject which would be navigated by MuWNS in this experiment was a person (labeled here as a navigatee). The navigatee first placed the receiver detector underneath the second reference detector located on the second floor (Figure 1A). Then the navigatee held the muPS receiver detector and moved to the basement floor using an elevator. Due to the limited near-horizontal muon flux and the resultant smaller effective area, navigation between the sixth floor and the basement floor was not conducted. In the first measurement phase, the navigatee traveled from the north to the south sides of the building along the corridor of the basement and subsequently traveled back from the south to north sides of the building (red arrow in Figure 1). Subsequently, the navigatee came back to the sixth floor and placed the reference detector back underneath the second reference detector to measure the drift level between the start and the end of the measurements to calculate the drift level of the receiver's clock for correction of the acquired data. In the second measurement phase, the navigatee traveled from the east to the west. The results of the second measurement phase will be described later.

The time required for the entire process of this measurement (one round trip) was within 30 min. As can be seen in Figure 2, since it is reasonable to assume that the frequency drift exists as a linear function of time within 30 min after the GMC is disconnected from the GNSS antenna, the frequency drift during navigation was estimated by interpolating the drift level between beginning and ending of the measurements. The position of the origin of the coordinate (x, y, z) = (0, 0, 0) was taken on the sixth floor of the building as indicated in Figure 1. The actual path of the navigatee is indicated with red arrows in Figure 1, and the muometrically determined path in the current work is indicated with blue and white lines. In this plot, for the reconstruction of the muometric path, the vertical displacement (z) was fixed to be 0 m and −24 m. More detailed descriptions about the results will be described in the following sections.

Navigation results

The second reference detector (reference 2 in Figure 1) that is connected to the GPS-disciplined clock was used for calibration of the receiver detector before navigation and after navigation. Since local clock associated with the receiver detector drifts, the time offset generated during navigation was estimated by comparing the GPS-disciplined clock before and after navigation. Figure 4 shows the TOF of muons at the initial position. From this figure, a short-term (~10 s) jitter level in the timing of the current navigation

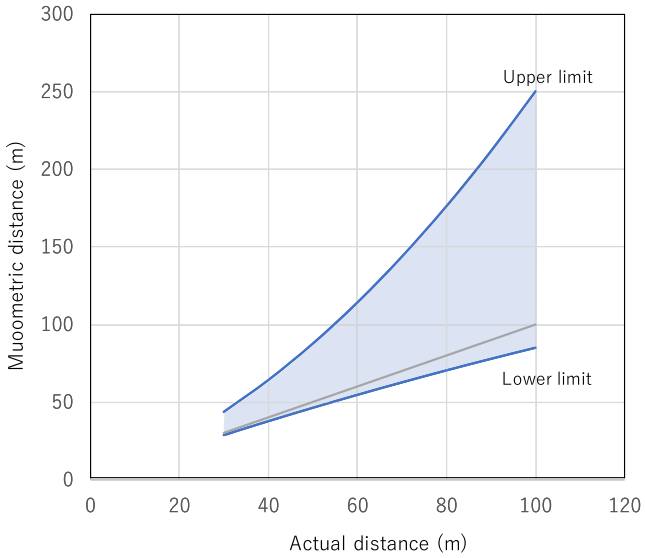

Figure 5. Accuracy degradation in L_i due to accidental coincidence

The upper limit (100%) and the lower limit (100%) (blue lines) in muometrically determining the distance (L_i) between the reference detector and the receiver detector are shown. Gray lines show the distance without metric errors.

system can be estimated, and the results were ~5 ns (1 standard deviation [SD]) and ±15 ns (peak to peak). The most dominant factor to generate this jitter is caused by fluctuations of the OCXO's frequency. The second-most dominant factor comes from fluctuations of the location where the muons hit on the scintillator (±3 ns peak to peak). The distance between the second reference detector and the receiver detector was 50 cm; therefore, the expected mean value for TOF in Figure 4A is ~1.5 ns, which is sufficiently smaller than the jitter of the current system.

Figure 5 shows the relationship between the accuracy degradation in determining $L_{\mu i}$ due to accidental coincidence and the distance between the receiver detector and the reference detector. Considering the limited muon flux due to small solid angles, which are made between the reference detector and the receiver detector as shown in Equation 2, the rate of accidental coincidence of single counts may exceed the muon-tracking rate for positioning. In the current case, since the open-sky single count rate is $\sim 10^2$ Hz, the coincidence time window of 1 us causes an accidental coincidence rate of $\sim 10^{-2}$ Hz. On the other hand, the muon-tracking rate will be degraded to $\sim 10^{-2}$ Hz, when the distance between the reference detector and the receiver detector exceeds 100 m. For this reason, a navigation measurement was not performed when $L_i \gtrsim 100$ m. The TOF shorter than 50 ns indicates a traveling distance of 15 m at a speed of light. This distance is much shorter than the baseline length we handled in this work; thus, such TOF data were discarded from the current analysis (T_{CUT}). Considering the flat probabilistic distribution of the accidental coincidence as a function of time, its contribution to the TOF data shorter than 50 ns is small, which was only 2.2% of the entire events selected within the time window of 1 us. However, in order to improve the navigation quality, these data were also removed from the current analysis. Although this process does not remove all of the accidental coincidence events and remaining accidental coincident events may degrade the positioning accuracy, it was anticipated that their contribution was largely mitigated by this process. The upper and lower limits were calculated in the following way:

(A) calculate the muon TOF between the reference and receiver by giving L_i,

(B) calculate the muon tracking rate by giving S,

(C) calculate the accidental event rate from $f_{ACCIDENT} = 2f_\mu{}^2 T_w$, where f_μ is the single muon rate and T_w is the coincidence time window for tracking muons,

(D) calculate the accidental event ratio ($R_{ACCIDENT}$) from $f_{ACCIDENT}/f_\mu$,

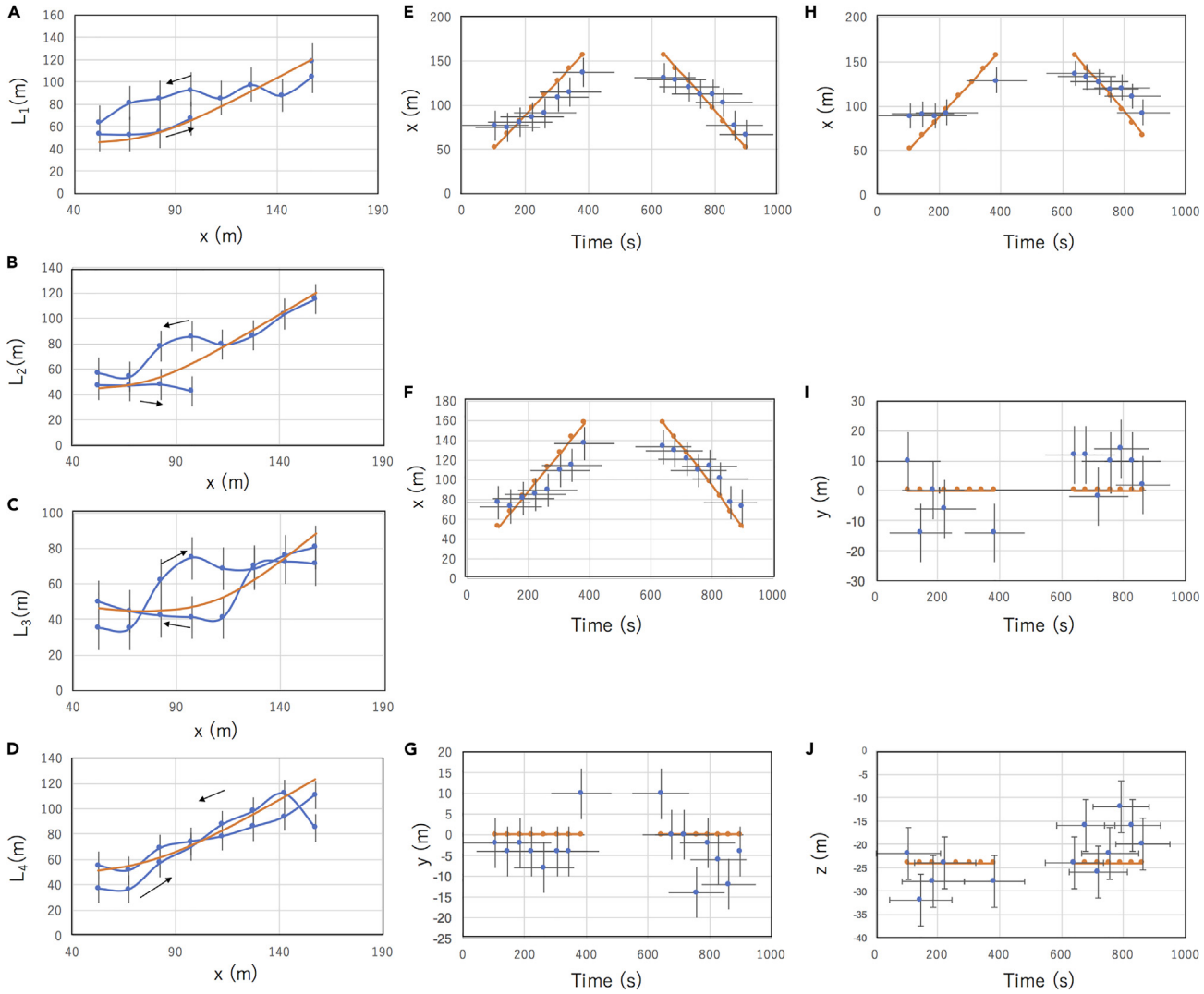

Figure 6. Results of indoor muometric navigation in the direction of N–S

(A–J) Muometrically measured distances ($L_{\mu i}$) (orange data points) and the theoretically calculated distances (L_i) (blue lines) between the four reference detectors and the receiver detector as a function of the distance (x) from the north edge of the building are shown (A–D). Orange lines are Bézier curves[39] corresponding to the data points. Blue arrows and red arrows both indicate the navigatee's directions of movement. The positioning results (orange data points) are shown for when: y, z, and t were fixed (1D) (E), when z and t were fixed (2D) (F and G), and when t was fixed (3D) (H–J). Blue data points indicate the actual position of the navigatee. Blue lines are Bézier curves corresponding to the data points. Error bars indicate one standard deviation of uncertainty.

(E) calculate the upper limit of the muon TOF from $R_{ACCIDENT}L_ic^{-1}T_W$ by assuming all of the muon TOF generated by the accidental events is T_W, and

(F) calculate the upper limit of the muon TOF from $R_{ACCIDENT}L_ic^{-1}T_{CUT}$ by assuming all of the muon TOF generated by the accidental events is T_{CUT}.

Figures 6A–6D all compare the muometrically measured distances ($L_{\mu i}$) and the theoretically calculated distances (L_i) between four reference detectors and the receiver detector as a function of the horizontal distance (x) from the north edge of the building. The muon data were moving-averaged over the spatial widow of 75 m with an interval of 15 m; namely, they were averaged over 15–90 m, 30–105 m, 45–120 m, and so on, and mean distances were compared between the actual values and the muometrically determined values and were compared with the moving average positions weighted by the number of recorded muons per unit distance in the following way:

$$\langle x_{ij} \rangle = \frac{\sum_{k=1}^{n} x_k}{n} \quad \text{(Equation 5)}$$

where $<x_{ij}>$ is the weighted position averaged over the range between x_i and x_j; x_k indicates the position where a muon was recorded; and n is the total number of muons recorded within the range between x_i and x_j. However, there were still zero-data periods due to substantially low muon arrival frequency. Such a significant reduction in the muon flux was probably caused by massive materials (such as mass spectroscopy machines) obstructing the muon path between the reference detectors and receiver detector (see Principle section). Each concrete floor thickness is 30 cm. Considering the typical density of a reinforced concrete slab is 3 gcm^{-3}, the total thickness of the overburden is 5.4 m water equivalent (m.w.e.) that is equivalent to E_c = 1 GeV. If a steel-made material with a thickness of 1 m is added, E_c increases to ~3 GeV. As a consequence, vertical integral muon flux is reduced by half (from ~60 $m^{-2}s^{-1}sr^{-1}$ to ~30 $m^{-2}s^{-1}sr^{-1}$). In Figure 6, the theoretically calculated L_i values are overlain. The SD of the muometric lengths from the theoretical lengths was 15.4 m, 13.8 m, 13.4 m, and 10.2 m for $L_{\mu 1}$, $L_{\mu 2}$, $L_{\mu 3}$, and $L_{\mu 4}$, respectively.

Based on the muometrically determined $L_{\mu i}$, x, y, and z positions of the navigatee, calculations were performed by using Equation 1. In the current work, t was fixed. The results are shown in Figures 6E–6J. The error bars associated with data points indicate an SD from the actual positions. Figure 6E presents the result when y, z, and t were fixed while Figures 6F–6J respectively indicate the results when z and t were fixed and results when only t was fixed. During the course of the current calculation of the position reconstruction, the range of x, y, and z was limited roughly within the dimension of the building, namely 0 m < x < 200 m, −15 m < y < 15 m, and −36 m < z < −12 m. As a result, the best performance (13.7 m as the minimum SD) to determine x positions of the navigatee was achieved when z and t were fixed. It is worth stating here that in Figure 6G, the muometrically derived positions are systematically deviated to the positive y directions. Since it was difficult for us to directly measure the y-directional spatial displacements between the N-S corridor on the basement floor and another N-S corridor on the sixth floor where origin of coordinates was set, it was assumed that there was no y-directional spatial displacement between them. However, as can be seen in Figure 1, the basement N-S corridor is located at the center, and the N-S corridor on the sixth floor is shifted toward the east. If we roughly estimate the y-directional spatial displacements between these corridors from these schematics, it is ~10 m that is in agreement with the muometrically derived positions.

Although a corridor running in the N-S direction was available on the basement floor, there was no E-W pathway inside the building. In order to evaluate the MuWNS positioning accuracy in the E-W direction, a pathway (which was located outside and parallel to the short side of the building) was used (see Figure 3). Since the reference detectors were located inside the building, the muons used for navigation would have to first pass through the building before arriving at the receiver detector. Therefore, this experiment provides a reasonable demonstration of the indoor navigation in the E-W direction. The navigation results are shown in Figure 7. Figures 7A–7D compare the muometrically measured distances ($L_{\mu i}$) and the theoretically calculated distances (L_i) between four reference detectors and the receiver detector as a function of the horizontal distance (x) from the north edge of the building. The muon data were moving-averaged over the spatial distance widow of 90 m with an interval of 30 m, and mean distances were compared between the actual values and the muometrically determined values. The theoretically calculated L_i values are overlain. The standard deviation of the muometric lengths from the theoretical lengths was 12.1 m, 22.8 m, 22.9 m, and 12.8 m for $L_{\mu 1}$, $L_{\mu 2}$, $L_{\mu 3}$, and $L_{\mu 4}$, respectively. Likewise, calculations of the x, y, and z positions of the navigatee were performed by using Equation 1. The results are shown in Figures 7E–7J. Figure 7E presents the result generated when y, z, and t were fixed while Figures 7F–7J respectively indicate the results when z and t were fixed and the results when only t was fixed. During the course of the current calculation of the position reconstruction, the range of x, y, and z was limited roughly within the dimension of the building, namely −50 m < x < 150 m, −15 m < y < 15 m, and −15 m < z < 15 m. As a result, the best performance (12.4 m as the minimum SD) to determine the x positions of the navigatee was achieved when z and t were fixed.

DISCUSSION

As the first step of the practical implementation of wireless muPS, it has been shown that MuWNS enables navigation in indoor/underground environments with similar or slightly more precise levels of accuracy as single-point GNSS/GPS positioning in urban areas. Satellite positioning systems can be vulnerable to

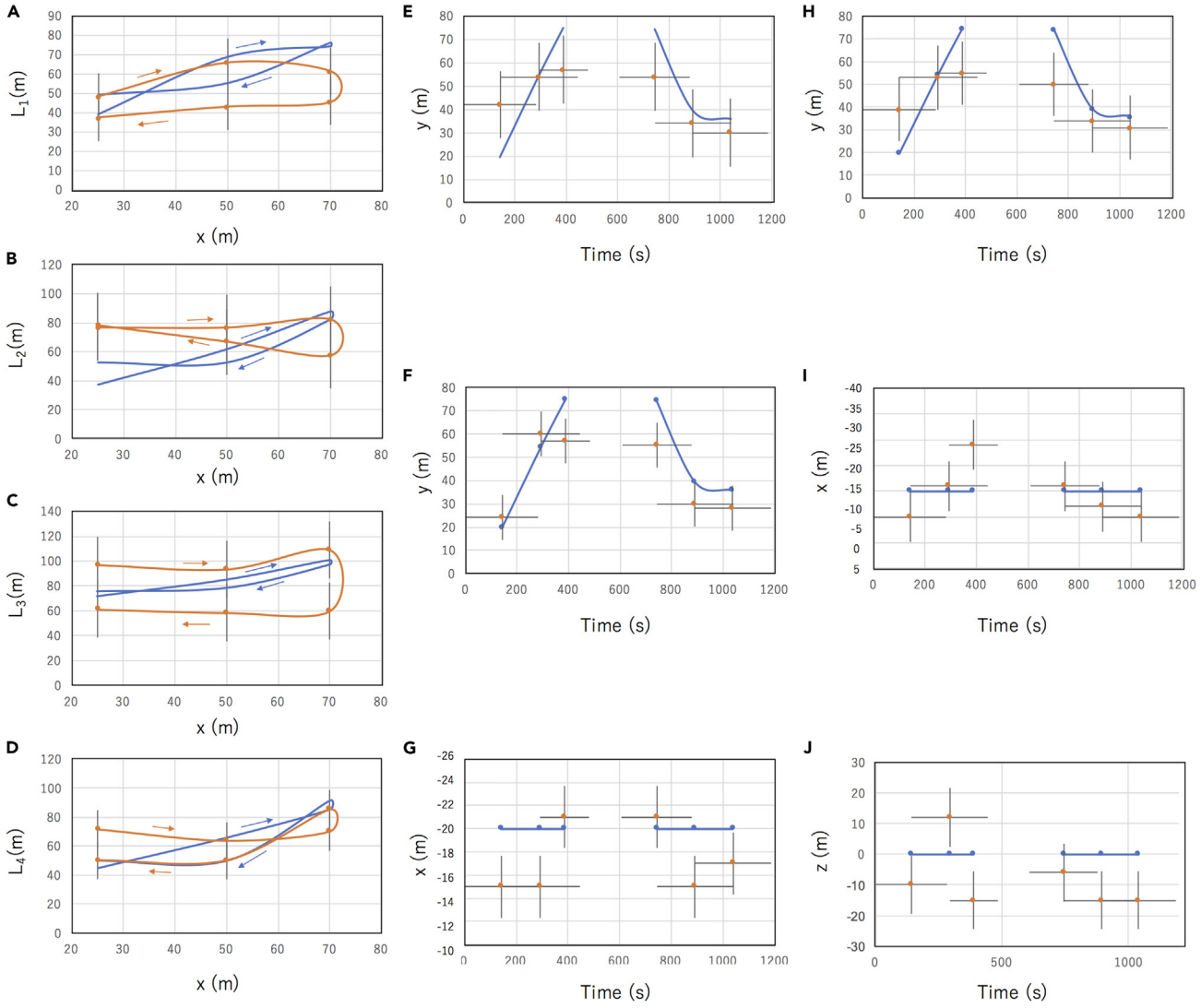

Figure 7. Results of indoor muometric navigation in the direction of E–W

(A–J) Muometrically measured distances ($L_{\mu i}$) (orange data points) and the theoretically calculated distances (L_i) (blue lines) between the four reference detectors and the receiver detector as a function of the distance (x) from the north edge of the building are shown (A–D). Orange lines are Bézier curves corresponding to the data points. Blue arrows and red arrows both indicate the navigatee's directions of movement. The positioning results (orange data points) are shown for when: y, z, and t were fixed (1D) (E), when z and t were fixed (2D) (F and G), and when t was fixed (3D) (H–J). Blue data points indicate the actual position of the navigatee. Blue lines are Bézier curves corresponding to the data points. Error bars indicate one standard deviation of uncertainty.

knockout from solar activity or possibly hostile acts. This new system never switches off. Therefore, it was concluded that MuWNS could serve as an alternative positioning system in regions where GNSS/GPS signals were unavailable. In Table 1, the positioning accuracy is compared between the current work and the results of single-point GNSS/GPS positioning in urban areas.

In the current work, real-time navigation was not performed. Since the OCXO's drift level was estimated by comparing the TOF data collected at the beginning and the ending of the measurements, all of the navigation results presented here were obtained after the offline analysis. In the current situation, if the 4-fold equations in Equation 1 are solved directly in real time, since the jitter and the drift level are both high (jitters of $\pm$15 ns [peak to peak] and drifts of ~300 ns in 30 min), the positioning accuracy will be significantly degraded. More stable clocks will be needed for both accurate real-time navigation and improved positioning accuracy. The easiest solution to achieve this would be to use double OCXOs (DOCXOs). This cheap and simple adaptation would improve the situation by a factor of 1.4. However, in order to attain our

Table 1. Comparison between the currently achieved MuWNS positioning accuracy and single-point GNSS/GPS positioning in urban areas reported in prior works

Technique	1 SD error (m) (N-S/E-W)	Max (m) (N-S/E-W)
MuWNS		
Horizontal (x) (Tokyo) (3D)	16.1/4.85	28.3/9.0
Horizontal (y) (Tokyo) (3D)	5.0/14.07	6.0/24.21
Vertical (Tokyo) (3D)	6.6/9.62	8.0/15.0
Horizontal (x) (Tokyo) (2D)	12.6/2.7	19.3/5.0
Horizontal (y) (Tokyo) (2D)	2.3/9.6	6.0/19.2
Horizontal (Tokyo) (1D)	11.4/13.9	22.0/22.4
GNSS/GPS		
Horizontal (Tokyo)[40]	16.1–47.9	102.5–290.7
Vertical (Tokyo)[40]	24.8–115.4	167.8–409.7
Horizontal (Calgary)[37]	9.4	54.8–97.0
Vertical (Calgary)[37]	7.5–15.1	41.1–204.7

final goal, real-time navigation with a positioning accuracy of 1 m, the specification of DOCXO is not enough.

How can this next step of MuWNS (a positioning accuracy of 1 m in real time) be achieved? The following three issues have to be overcome. In the current work, the positioning accuracy was limited to ~10 m. There are four factors that degrade positioning accuracy: (1) accidental coincidence events remaining in muPS data, (2) fluctuation in the local clock, (3) longer TOF due to non-relativistic muons, and (4) accidental coincidence due to the extended air shower. Regarding the first factor, one more redundant detector located between the reference detectors and the receiver detectors would drastically reduce the accidental coincidence rate by selecting only 3-fold coincidence events among the reference detectors, the redundant detector, and the receiver detector. However, placing one more detector is not practical for navigation. Shortening the coincidence time window (T_W) might be more practical. This would be possible by employing more stable local clocks as described later. Regarding the second factor, frequency fluctuations can be seen in Figure 2. These fluctuations are up to $\pm$50 ns and increase uncertainty in positioning accuracy up to 30 m. Degradation of the positioning accuracy associated with this kind of problem could be mitigated by using clocks much more stable than OCXO, for example, Cs oscillators. Recently small electronics-chip scale Cs oscillators are being developed. If we use a Cs oscillator instead of OCXO, the jitter and the drift level would be mostly suppressed (<7 ns/day) and more stable which would enable more accurate positioning and a narrower coincidence time window. Such oscillators could be installed into muPS in the near future. Regarding the third factor, non-relativistic muons extend their TOF for a given traveling distance; hence the resultant muometric positions would erroneously indicate positions further away from the actual positions. In order to attain a positioning accuracy of 1 m for L_i = 100 m, detection of muons would be limited to those with a speed of more than 0.99c which would be equivalent to the muon's kinetic energy of 700 MeV. If we insert a lead shield with a thickness of 50 cm above the receiver detector, muons with energies less than 700 MeV could be rejected. However, the receiver detector's weight increases significantly, and thus this solution is not ideal for practical operations. However, only ~10% of all the muons at sea level have energies less than 700 MeV. Therefore, if we collect the TOF information from multiple events and take an average over these events, this problem may not be so critical at least for the purpose of attaining a positioning accuracy of 1 m. Regarding the fourth factor, time displacements between arrivals of the extended air shower (EAS) particles to the distant detectors depend on the horizontal distance between these detectors and ranged from 10 ns to 100 ns[35]. These time displacements are shorter than the time required for relativistic muons to travel a distance longer than 30 m; hence the resultant muometric positions would erroneously indicate positions closer to the actual positions. However, this EAS-associated positioning error affects only horizontal directions, not the vertical direction since EAS particles from the upper hemisphere continuously arrive. Therefore, as long as the position of the receiver detector (x, y, z) is located within a range of x < z and y < z, this EAS-associated positioning error is mitigated and negligible for at least the purpose of attaining the positioning accuracy of 1 m.

Table 2. Pros and cons of various indoor/underground navigation techniques

Technique	Current Accuracy (m)	Range (m)	Pros	Cons
MuWNS (Current work)	2-25 m	30-100 m	Environment-free	Low time resolution
RFID[10]	10-30 m	1 m	Control center required	No battery required
ZigBee[10]	10-200 m	1-75 m	Wi-Fi network required	Low power consumption
Lidar[11]	0.2 m	3-12 m	High accuracy	Clear views required
Acoustic[5]	0.01–3 m	A few m	High accuracy	Clear views required

Unlike other camera-based indoor/underground navigation systems, the navigation capability of MuWNS is not restricted by the ambient conditions, such as brightness, availability of landmarks, Wi-Fi signals, etc, and in principle, errors do not accumulate as the time span of the navigation session lengthens. Thus, recurrent corrections are not necessary. As long as the local clock's jitter level is sufficiently suppressed, the time offset coming from the intrinsic drift of MuWNS can be corrected by solving Equation 1. Moreover, the intrinsic drift of MuWNS is not associated with the principle of muPS and can be improved by future improvements of local clock design used for time synchronization between the reference detectors and the receiver detector. On the other hand, more fundamental problems associated with MuWNS come from the characteristics of the naturally occurring muon flux. Since the number of open-sky muons is limited to $\sim 10^2\ m^2\ s^{-1}\ sr^{-1}$, the detector size tends to be larger than a typical compact GNSS/GPS unit, and the time required for positioning is extended as a function of square of the distance between the reference detectors and the receiver detector. This probably limits the size of the navigational area. In Table 2, pros and cons of the indoor/underground navigation techniques are compared. Consequently, it was found that MuWNS could potentially be the best positioning performance in dark, obstructive indoor/underground environments.

For the purpose of navigation, since there is an interest in being as quick as possible, hence not waiting for more muons, four muons are the minimum number required to solve the basic equations shown in Equation 1. However, for the purpose of positioning (not navigation), one can afford to take more muons to overconstrain the equations and get more precision. For example, for the purpose of monitoring seafloor deformation due to submarine volcano activities, more muons can be collected. In this case, since receiver detectors are not expected to actively move, reference detectors and receiver detectors can be wired for more accurate synchronization. A possible scenario and expected positioning accuracy can be found in Tanaka (2020)[18] for muPS equipped with a GPS buoy.

In conclusion, the first physical underground/indoor MuWNS navigation has been successfully completed. Positioning accuracy was 2–25 m depending on the navigation direction and the distance between the reference detectors and the receiver detector. The currently achieved positioning accuracy was comparable or slightly better than the positioning accuracy attainable with single-point GNSS/GPS positioning in urban areas. The current limitation of the positioning accuracy mainly comes from instability of the local clocks, and thus we anticipate that replacement of the current clocks with more stable clocks, for example with Cs oscillators, will improve the positioning accuracy. With these new results, it is clear that with further improvements, MuWNS can be adapted to improve autonomous mobile robot navigation, positioning, and other underground and underwater practical applications. As natural resource explorations, automated resilient societies and the need to better understand Earth geological/climate systems continue to become more urgent concerns to world economies, muPS is a new tool with unique characteristics that give it the potential to contribute to research in these topics.

Limitations of the study

In the current work, the positioning accuracy was limited to ~10 m. There are four factors that degrade positioning accuracy: (1) accidental coincidence events remaining in muPS data, (2) fluctuation in the local clock, (3) longer TOF due to non-relativistic muons, and (4) accidental coincidence due to the extended air shower.

STAR★METHODS

Detailed methods are provided in the online version of this paper and include the following:

- KEY RESOURCES TABLE

ACKNOWLEDGMENTS

We would like to thank the Institute of Industrial Science (University of Tokyo) for use of their building for the current experiment.

AUTHOR CONTRIBUTIONS

HKMT wrote the manuscript. HKMT prepared figures and tables. All reviewed the manuscript.

DECLARATION OF INTERESTS

The authors declare no competing interests.

Received: July 22, 2022
Revised: April 20, 2023
Accepted: May 24, 2023
Published: May 29, 2023

REFERENCES

1. Kosaka, A., and Kak, A.C. (1992). Fast vision-guided mobile robot navigation using model-based reasoning and prediction of uncertainties. Comput. Vis. Image Underst. *56*, 271–329.
2. Lu, F., and Milios, E. (1997). Robot pose estimation in unknown environments by matching 2D range scans. J. Intell. Robot. Syst. *18*, 249–275.
3. Hakim, S. (1997). A mobile system for indoors 3-D mapping and positioning. Proc. 4th Conf. Optical 3-D Meas. Techn. 275–282.
4. Motomura, A., Matsuoka, T., Hasegawa, T., and Kurazume, R. (2005). Real-time self-localization method by using measurements of directions of two landmarks and dead reckoning. J. Robot. Soc. Jpn. *23*, 311–320.
5. Sertatıl, C., Altınkaya, M.A., and Raoof, K. (2012). A novel acoustic indoor localization system employing CDMA. Digit. Signal Process. *22*, 506–517.
6. Hahnel, D., Burgard, W., and Thrun, S. (2001). Learning compact 3d models of indoor and outdoor environments with a mobile robot. Proc. 4th EUROBOT, 91–98.
7. Kelly, A. (2001). General solution for linearized systematic error propagation in vehicle odometry. Proc. IEEE/RSJ IROS, 1938–1945.
8. Crowley, J.L. (1989). Asynchronous control of orientation and displacement in a robot vehicle. Proc. IEEE Int. Conf. Robot. Autom. 1277–1282.
9. G. Corporation (2022). About GPS. http://www.garmin.com/aboutGPS/.
10. Kataria, S., Singh, P., and Ahlawat, P. (2015). Survey paper on wireless underground positioning system. Int. J. Comput. Appl. *130*, 1–4.
11. Chow, J.F., Kocer, B.B., Henawy, J., Seet, G., Li, Z., Yau, W.Y., and Pratama, M. (2019). Toward underground localization: lidar inertial odometry enabled aerial robot navigation. Preprint at arXiv. https://doi.org/10.48550/arXiv.1910.13085.
12. Moravec, H.P. (1996). Robot Spatial Perception by Stereoscopic Vision and 3d Evidence Grids (Pittsburgh, PA, Tech. Rep.: Robot. Inst., Carnegie Mellon Univ.). CMU-RI-TR-96-34.
13. Meng, M., and Kak, A.C. (1993). NEURO-NAV: a neural network based architecture for vision-guided mobile robot navigation using non-metrical models of the environment. Proc. IEEE Int'l Conf. Robotics and Automation *2*, 750–757.
14. Meng, M., and Kak, A.C. (1993). Mobile robot navigation using neural networks and nonmetrical environment models. IEEE Control Syst. Mag. 30–39.
15. Pan, J., Pack, D.J., Kosaka, A., and Kak, A.C. (1995). FUZZY-NAV: a vision-based robot navigation architecture using fuzzy inference for uncertainty-reasoning. Proc. IEEE World Congress Neural Networks *2*, 602–607.
16. Drocourt, C., Delahoche, L., Pegard, C., and Clerentin Gracsy, A. (1999). Mobile robot localization based on an omni directional stereoscopic vision perception system. Proc. Int. Conf. Robot. Autom. 1329–1334.
17. Betke, M., and Gurvits, L. (1997). Mobile robot localization using landmarks. IEEE Trans. Rob. Autom. *13*, 251–263.
18. Tanaka, H.K.M. (2020). Muometric positioning system (μPS) with cosmic muons as a new underwater and underground positioning technique. Sci. Rep. *10*, 18896. https://doi.org/10.1038/s41598-020-75843-7.
19. Tanaka, H.K.M. (2022). Wireless muometric navigation system. Sci. Rep. *12*, 10114. https://doi.org/10.1038/s41598-022-13280-4.
20. Tanaka, H., Nakano, T., Takahashi, S., Yoshida, J., Takeo, M., Oikawa, J., Ohminato, T., Aoki, Y., Koyama, E., and Tsuji, H. (2007). High resolution imaging in the inhomogeneous crust with cosmic-ray muon radiography: the density structure below the volcanic crater floor of Mt. Asama, Japan. Earth Planet Sci. Lett. *263*, 104–113.
21. Kusagaya, T., and Tanaka, H.K.M. (2015). Muographic imaging with a multi-layered telescope and its application to the study of the subsurface structure of a volcano. Proc. Jpn. Acad. Ser. B *91*, 501–510.

22. Oláh, L., Tanaka, H.K.M., Ohminato, T., and Varga, D. (2018). High-definition and low-noise muography of the Sakurajima volcano with gaseous tracking detectors. Sci. Rep. *8*, 3207. https://doi.org/10.1038/s41598-018-21423-9.

23. Nomura, Y., Nemoto, M., Hayashi, N., Hanaoka, S., Murata, M., Yoshikawa, T., Masutani, Y., Maeda, E., Abe, O., and Tanaka, H.K.M. (2020). Pilot study of eruption forecasting with muography using convolutional neural network. Sci. Rep. *10*, 5272. https://doi.org/10.1038/s41598-020-62342-y.

24. Oláh, L., Tanaka, H.K.M., and Hamar, G. (2021). Muographic monitoring of hydrogeomorphic changes induced by post-eruptive lahars and erosion of Sakurajima volcano. Sci. Rep. *11*, 17729. https://doi.org/10.1038/s41598-021-96947-8.

25. D'Errico, M., Ambrosino, F., Anastasio, A., Basnet, S., Bonechi, L., Bongi, M., Bross, A., Ciaranfi, R., Cimmino, L., Ciulli, C., et al. (2022). The MURAVES experiment: study of the vesuvius great cone with muon radiography. Preprint at arXiv. https://doi.org/10.48550/arXiv.2202.12000.

26. Tioukov, V., Alexandrov, A., Bozza, C., Consiglio, L., D'Ambrosio, N., De Lellis, G., De Sio, C., Giudicepietro, F., Macedonio, G., Miyamoto, S., et al. (2019). First muography of Stromboli volcano. Sci. Rep. *9*, 6695. https://doi.org/10.1038/s41598-019-43131-8.

27. Lo Presti, D., Riggi, F., Ferlito, C., Bonanno, D.L., Bonanno, G., Gallo, G., La Rocca, P., Reito, S., and Romeo, G. (2020). Muographic monitoring of the volcano-tectonic evolution of Mount Etna. Sci. Rep. *10*, 11351. https://doi.org/10.1038/s41598-020-68435-y.

28. Shinohara, H., and Tanaka, H.K. (2012). Conduit magma convection of a rhyolitic magma: constraints from cosmic-ray muon radiography of Iwodake, Satsuma-Iwojima volcano, Japan. Earth Planet Sci. Lett. *349–350*, 87–97.

29. Jourde, K., Gibert, D., Marteau, J., de Bremond d'Ars, J., and Komorowski, J.C. (2016). Muon dynamic radiography of density changes induced by hydrothermal activity at the La Soufrière of Guadeloupe volcano. Sci. Rep. *6*, 33406. https://doi.org/10.1038/srep33406.

30. Noli, P., Ambrosino, F., Bonechi, L., Bross, A., Cimmino, L., D'Alessandro, R., Masone, V., Mori, N., Passeggio, G., Pla-Dalmau, A., et al. (2017). Muography of the Puy de Dôme. Ann. Geophys. *60*, S0105.

31. Morishima, K., Kuno, M., Nishio, A., Kitagawa, N., Manabe, Y., Moto, M., Takasaki, F., Fujii, H., Satoh, K., Kodama, H., et al. (2017). Discovery of a big void in Khufu's Pyramid by observation of cosmic-ray muons. Nature *552*, 386–390. https://doi.org/10.1038/nature24647.

32. Procureur, S., Morishima, K., Kuno, M., Manabe, Y., Kitagawa, N., Nishio, A., Gomez, H., Attié, D., Sakakibara, A., Hikata, K., et al. (2023). Precise characterization of a corridor-shaped structure in Khufu's Pyramid by observation of cosmic-ray muons. Nat. Commun. *14*, 1144. https://doi.org/10.1038/s41467-023-36351-0.

33. Saracino, G., Amato, L., Ambrosino, F., Antonucci, G., Bonechi, L., Cimmino, L., Consiglio, L., Alessandro, R.D., Luzio, E.D., Minin, G., et al. (2017). Imaging of underground cavities with cosmic-ray muons from observations at Mt. Echia (Naples). Sci. Rep. *7*, 1181. https://doi.org/10.1038/s41598-017-01277-3.

34. Cimmino, L., Baccani, G., Noli, P., Amato, L., Ambrosino, F., Bonechi, L., Bongi, M., Ciulli, V., D'Alessandro, R., D'Errico, M., et al. (2019). 3D muography for the search of hidden cavities. Sci. Rep. *9*, 2974. https://doi.org/10.1038/s41598-019-39682-5.

35. Tioukov, V., Morishima, K., Leggieri, C., Capriuoli, F., Kitagawa, N., Kuno, M., Manabe, Y., Nishio, A., Alexandrov, A., Gentile, V., et al. (2023). Hidden chamber discovery in the underground Hellenistic necropolis of Neapolis by muography. Sci. Rep. *13*, 5438. https://doi.org/10.1038/s41598-023-32626-0.

36. Tanaka, H.K.M. (2022). Cosmic time synchronizer (CTS) for wireless and precise time synchronization using extended air showers. Sci. Rep. *12*, 7078. https://doi.org/10.1038/s41598-022-11104-z.

37. Angrisano, A., Gaglione, S., and Gioia, C. (2013). Adaptive estimation of measurement noise to improve the performance of GNSS single point positioning in dense urban environment. Acta Geod. Geophys. *48*, 149–161.

38. Trimble. (2020). THUNDERBOLT PTP GM200 IEEE-1588 GRANDMASTER CLOCK NTP TIME SERVER. https://infocom.haradacorp.co.jp/wp/wp-content/uploads/2020/05/%E3%80%90GM200%E3%80%91UserGuide_v1.6.0.0.pdf.

39. Mortenson, M.E. (1999). Mathematics for Computer Graphics Applications, *264* (Industrial Press Inc)9780831131111.

40. Tominaga, T., and Kubo, N. (2017). Adaptive estimation of measurement noise to improve the performance of GNSS single point positioning in dense urban environment. Journal of IPNT *8*, 1–8.

STAR★METHODS

KEY RESOURCES TABLE

REAGENT or RESOURCE	SOURCE	IDENTIFIER
Other		
PMT	Hamamatsu Photonics	R7724
Plastic scintillator	Eljen Technology	EJ-200
TDC	ScioSense	GPX
GPS-DO	Trimble	Thunderbolt GM200

RESOURCE AVAILABILITY

Lead contact

Further information and requests for resources and reagents should be directed to and will be fulfilled by the lead contact, Hiroyuki K.M. Tanaka (ht@eri.u-tokyo.ac.jp).

Materials availability

This study did not generate new unique reagents.

Data and code availability

The datasets used and/or analyzed during the current study available from the corresponding author on reasonable request.

EXPERIMENTAL MODEL AND SUBJECT DETAILS

Our study does not use experimental models typical in the life sciences.

METHOD DETAILS

Material preparation

Our study does not materials typical in the life sciences.

Experimental apparatus

See wireless muometric navigation system and experimental configuration sections.

Experimental procedure

See navigation results section.

QUANTIFICATION AND STATISTICAL ANALYSIS

There is no statistical analysis in this paper.

ADDITIONAL RESOURCES

We have no relevant resources.